Temporal variability of ground-shaking and stress drop in central Italy: a hint for fault healing?

D. Bindi(1), F. Cotton(1,2), D. Spallarossa(3),
M. Picozzi(4), and E. Rivalta(1)
(1) German Research Centre for Geosciences GFZ, Potsdam, Germany;
(2) also at University of Potsdam, Potsdam, Germany
(3) University of Genova, DISTAV, Genova, Italy;
(4) University Federico II, Napoli, Italy;

June 1, 2018

- Dino Bindi, German Research Centre for Geosciences GFZ, Telegrafenberg, Helmholtzstrasse 6, 14467 Potsdam, Germany; bindi@gfz-potsdam.de
- Fabrice Cotton, German Research Centre for Geosciences GFZ, Telegrafenberg, Helmholtzstrasse 6, 14467 Potsdam, Germany; fcotton@gfz-potsdam.de
- Daniele Spallarossa, University of Genova, DISTAV, Viale Benedetto XV 5, 16132 Genova, Italy; daniele@dipteris.unige.it

- Matteo Picozzi, University Federico II, Via Cintia, 80126 Napoli, Italy; matteo.picozzi@unina.it
- Eleonora Rivalta, German Research Centre for Geosciences GFZ, Telegrafenberg, Helmholtzstrasse 6, 14467 Potsdam, Germany; rivalta@gfz-potsdam.de

Abstract

Ground Motion Prediction Equations (GMPEs) are calibrated to predict the intensity of ground shaking at any given location, based on earthquake magnitude, source-to-site distance, local soil amplifications and other parameters. GMPEs are generally assumed to be independent of time; however, evidence is increasing that large earthquakes modify the shallow soil conditions and those of the fault zone for months or years. These changes may affect the intensity of shaking and result in time-dependent effects that can potentially be resolved analyzing between-event residuals (residuals between observed and predicted ground motion for individual earthquakes averaged over all stations). Here we analyze a data set of about 65000 recordings for about 1400 earthquakes in the moment magnitude range 2.5-6.5 occurred in central Italy from 2008 to 2017 to capture the temporal variability of the ground shaking at high frequency. We first compute for each earthquake between-event residuals in the Fourier domain with respect to a ground motion prediction equation developed ad-hoc for the analyzed data set. The between-events show large changes after the occurrence of mainshocks such as the Mw 6.3, 2009 L' Aquila, the 2016, Mw 6.2 Amatrice and Mw 6.5

Norcia earthquakes. Within the time span of a few months after the mainshocks, the between-event contribution to the ground shaking varies by a factor 7. In particular, we find a large drop in the between-events in the aftermath of the l'Aquila earthquake, followed by a slow positive trend that leads to a recovery interrupted by a new drop at the beginning of 2014. We also quantify the frequency-dependent correlation between the Brune stress-drop $\Delta\sigma$ and the between-events. We find that the temporal changes of $\Delta\sigma$ resemble those of the between-event residuals; in particular, during the period when the between-events show the positive trend, the average logarithm of $\Delta\sigma$ increases with an annual rate of 0.19 (i.e., the amplification factor for $\Delta\sigma$ is 1.56 per year). Breakpoint analysis located a change in the linear trend coefficients of $\Delta\sigma$ versus time in February 2014 although no large earthquakes occurred at that time. Finally, the temporal variability of $\Delta\sigma$ mirrors the relative seismic velocity variations observed in previous studies for the same area and period, suggesting that both crack-healing along the main fault system and healing of micro-cracks distributed at shallow depths throughout the surrounding region might be necessary to explain the wider observations of post-earthquake recovery.

Introduction

The intensity of seismic shaking at a given site is a function of the earthquake size, style of faulting, source-to-site distance and site condition. Ground motion prediction equations (GMPEs) incorporate these functional dependencies and are time-independent, meaning that the intensity of shaking is

assumed to be independent of any process affecting the fault zone. However, some observations suggest that shaking intensity changes depending on the timing of earthquakes within sequences. For example, it has been observed that aftershocks generate lower median ground motion in the high frequencies (e.g., Boore and Atkinson 1989) and, therefore, they have been flagged in the recent NGA-West2 strong motion data set (Wooddell and Abrahamson, 2014) allowing GMPE developers to treat them differently from mainshocks. Some of the variability in the observed shaking may be explained by variability in the stress drop (e.g., Wu and Chapman, 2017). Analyzing the NGA-West2 data, Baltay and Hanks (2014) found that average stress drop for mainshocks is 30% larger than the average stress drop for aftershocks.

Identifying repeating deviations from the medial model can help distinguish processes that are not modeled but contribute significantly to ground motion variability. For example, several studies correlated earthquake-specific residuals (also called between-event or inter-event) to stress drop variability (e.g., Anderson and Lei, 1994; Bindi et al., 2007; Cotton et al., 2013; Oth et al., 2017; Bindi et al., 2017; Baltay et al., 2017; Ameri et al., 2017; Trugman and Shearer, 2018). Therefore, presence of any temporal pattern in the distribution of residuals can be used as diagnostic of time-dependent fault or medium properties, and ultimately help understanding how non-stationary processes, such as protracted seismic sequences or the long precursory phase of large earthquakes, affect ground motion. For example, Socquet et al (2016) and Piña-Valdés et al. (2018), in discussing the ground-shaking time-dependencies observed during the 2014 Iquique subduction sequence,

suggested that the temporal changes in the between-event residuals were associated with aseismic slip around the rupture area.

Here we take advantage of a large data set from central Italy to investigate the temporal changes of the between-event residuals and their link with the stress drop $\Delta\sigma$ variability. The data set includes about 1400 earthquakes in the magnitude range 2.5-6.5, belonging to the main sequences of the last ten years, i.e. the 2009 L'Aquila (Chiaraluce et al., 2011) and the 2016-17 Amatrice-Visso-Norcia (Chiaraluce et al., 2017) sequences. About 60 earthquakes occurred in area of the 2013-14 Gubbio swarm (De Gori et al., 2015) are included as well. We first calibrate an ad-hoc GMPE for the Fourier amplitude spectra and we evaluate the between-event residuals at different frequencies. Then, the between-event are used as exploratory tool to detect event-dependent temporal changes in the ground shaking and we conclude presenting the temporal variability of $\Delta\sigma$.

Data

In this study, we analyze about 65000 recordings (for each component of motion) from 1400 earthquakes recorded by 340 stations installed in Central Italy (Figure 1 and Figure S1 of the electronic supplements to this article). The earthquakes cover the magnitude range from 2.5 to 6.5 and hypocentral distances from 10 to 180 km are considered. The data set includes the main sequences occurred in the area in the last 10 years, namely the 2009, Mw 6.3 L'Aquila (indicated as e_1 in Figure 1); the 2016, Mw 6.1 Amatrice (e_2 in Figure 1); the 2016 Mw 6.1, Visso (e_4 in Figure 1); the 2016, Mw 6.5,

Norcia (e_3 in Figure 1) (for a map with the time evolution of the events, see Figure S2 in the electronic supplements to this article). Following Bindi et al. (2018), in this study we consider the moment magnitude from the Geofon catalog for all events with Mw $\geq$ 5.7 but the 2009, L'Aquila mainshock, for which we use the Global Centroid Moment Tensor (GCMT) value since the Geofon solution is not available (see the Data and Resources section). The data set also includes recordings from 59 earthquakes with magnitude larger than 2.5 occurred in the area of the 2013-14 Gubbio swarm; a complete description of the swarm is given by De Gori et al. (2015) and Valoroso et al. (2017). The station distribution is shown in Figure S1 in the electronic supplement to this article.

We analyse the Fourier amplitude spectra (FAS) of S-waves windows band-pass filtered with a variable high pass corner frequency depending on the signal-to-noise ratio. The Butterworth high-pass corner varies in the range 0.05−0.4 Hz while the low pass one was fixed to 40 Hz. The FAS are smoothed using the Konno and Ohmachi (1998) algorithm (the smoothing parameter b was set to 40). Details about the data selection and processing are provided by Pacor et al. (2016) and by Bindi et al. (2017).

Source parameters

For each earthquake, we consider the source parameter (i.e., stress drop and seismic moment) derived by Bindi et al. (2017) using a generalized inversion technique (GIT). In the GIT approach (e.g., Castro et al., 1990; Oth et al., 2011), the spectral values of a set of earthquakes recorded by a network of

stations are simultaneously inverted to isolate the contribution of source, propagation and site effects. The GIT approach exploits the redundancy of information (that is, the same earthquake is recorded at several stations located at different distances, and several earthquakes are recorded at the same station) to set-up an over-determined system of equations solved in a least-squares sense. To remove unresolved degrees of freedom which generate trade-offs among different components of the solution, some constraints are applied, such as the choice of a reference distance at which the attenuation is assumed to be one and a reference site condition (i.e., one or more stations whose site amplification is assumed to be known). In this study, we use the results of Bindi et al (2018) who applied a non-parametric GIT inversion where any a-priori seismological models for source and attenuation were adopted during the GIT inversion. To estimate the seismic moment and the corner frequency for each earthquake, the resulting non-parametric source spectra were fit to a Brune (1970) source model which assumes a circular fault with uniform stress drop. In Bindi et al. (2018), the source fit was performed allowing a deviation of the high frequency acceleration spectral level from a constant value as predicted by the Brune model. The high-frequency slope of the source spectrum is referred to as k_{source}. Given the seismic moment and the corner frequency, the stress drop was computed following Eshelby (1957) and Keilis-Borok (1959).

The source parameters are shown in Figure 2, in terms of scaling between $\Delta\sigma$, Mw and hypocentral depth. Most of the considered depths including those of the mainshocks are located between 5 and 10 km. The stress drop tends to increase with depth and has a strong magnitude dependence (Pacor

et al., 2016; Bindi et al. 2017). The mainshocks have the largest $\Delta\sigma$, around 10 MPa. The overall $\Delta\sigma$ variability covers almost three orders of magnitude. The procedure followed in this study to estimate the uncertainties on $\Delta\sigma$ is described in the electronic supplement to this article.

Ground motion model

In this study, we describe the Fourier amplitude spectra $FAS(f, R)$ at frequency f of S-waves recorded at hypocentral distance R with the following seismological model:

$$FAS(f,R) = S(f)\cdot P(f,R)\cdot Z(f) = K\frac{M_0 f^2}{1+(\frac{f}{f_c})^2}\cdot\frac{1}{R^n}exp(-\frac{\pi f R}{Q\beta})\cdot Z(f) \quad (1)$$

where the acceleration source spectra $S(f)$ is parametrized considering an ω-square model (Aki, 1967) and the spectral attenuation with distance $P(f, R)$ is controlled by the geometrical spreading exponent n and the anelastic attenuation, the latter being modeled through the quality factor $Q(f)$. In equation 1, the constant K depends on the density and velocity at the source location, on radiation pattern and free surface amplification effects, whereas $Z(f)$ accounts for site amplification effects. We only consider far-field source terms and extended-source effects are not accounted for. The asymptotic form of the source spectrum is as follow:

$$S(f) \propto \begin{cases} M_0 f_c^2 & \text{if } f \gg f_c \\ M_0 f^2 & \text{if } f \ll f_c \end{cases} \tag{2}$$

The source spectrum depends on two parameters, the seismic moment M_0 and the corner frequency f_c connected through the stress drop $\Delta\sigma$ (Brune, 1970; Eshelby, 1957) as follows:

$$\Delta\sigma \propto M_0 d^{-3} \propto M_0 f_c^3 \tag{3}$$

where d is the source radius. Considering equation 3, equation 2 can be re-written as:

$$S(f) \propto \begin{cases} M_0^{\frac{1}{3}} \Delta\sigma^{\frac{2}{3}} & \text{if } f \gg f_c \\ M_0 f^2 & \text{if } f \ll f_c \end{cases} \tag{4}$$

If the average stress drop of the analyzed earthquakes is assumed to be constant, the scaling of the source spectrum with the earthquake size is controlled only by the seismic moment (Aki, 1967). Under this assumption and considering a mixed effect regression (Bates et al., 2015), Equations 1 and 4 suggest the following parametric model for $FAS(f, R)$:

$$ln(FAS) = a_1 + a_2 Mw + a_3 ln(R) + a_4 R + \delta B_e + \delta B_s + \epsilon \tag{5}$$

where the moment magnitude Mw is proportional to $Log(M_0)$ (Hanks and Kanamori, 1979). In equation 5, the coefficients a_i are the (frequency dependent) fixed effects which define the median prediction; δB_e, δB_s are the

random effects for the earthquake and station grouping levels, respectively; ϵ is the residual distribution. In order to allow more complex scaling with magnitude, the functional form considered in this study is the following:

$$ln(FAS) = e_1 + b_1(Mw - M_{ref}) + b_2(M - M_{ref})^2 + [c_1 + c_2(M - M_{ref})]ln(\frac{R}{R_{ref}}) + c_3(R - R_{ref}) + \delta B_e + \delta B_s + \epsilon \quad (6)$$

with $M_{ref} = 3.5$ and $R_{ref} = 1km$. In equation (6), the fixed effect coefficients describe the scaling with distance (c_1 and c_3 are connected to the geometrical spreading attenuation and the quality factor, respectively) and with magnitude (b_1 and b_2 are controlling the scaling with the seismic moment). Coefficient c_2 introduces a magnitude dependency in the attenuation with distance, while the off-set e_1 depends (at high frequency) on source characteristics such as the average stress drop, among other quantities. The between-event δB_e quantifies the systematic deviation of recordings for the same event with respect the median prediction. At high frequencies, the deviation of the stress drop of any earthquakes from the average of the population is expected to contribute to the δB_e residuals while differences in the average radiation pattern among the earthquakes due to uneven station distribution can contribute to δB_e at low frequency (along with other factors such as differences in the density and velocity at the source location, errors in the magnitude values, etc). The between station δB_s random effects, sometimes referred to as $\delta S2S$, absorb the frequency dependent site amplification indicated with $Z(f)$ in equation 1.

The frequency-dependent coefficients of the model (6) and the standard

deviations of δB_e, δB_s, and ϵ are listed in Table S1 of the electronic supplement to this article. The residuals ϵ versus hypocentral distance and δBe versus magnitude are exemplified in Figure 3 for two frequencies. Over the intervals well constrained by data, the average residuals do not show systematic trends with the predictor variables but the variability of δB_e increases with frequency (see also Table S1). Weak trends at short distances (at high frequency) and for large magnitude (at low frequencies), which are not impacting on the analysis performed in this study, could be removed by introducing distance and magnitude hinges in equation (5).

Between-event temporal variability

The temporal trend of the between-event δB_e at 10 Hz is shown in Figure 4 while zooms over different time windows are presented in Figure S3 of the electronic supplement to this article. In addition to the large variability in the aftermath of the mainshock occurrence, the most striking feature in Figure 4 is the positive trend developing from the end of 2009, a few months later than the April 6, 2009 L'Aquila mainshock, to late 2013-early 2014. In the period from early 2014 to August 2016, when the Amatrice sequence started, δB_e shows a large variability with average value close to zero. When observed at low frequencies (Figure 4), δB_e shows a weak trend with time. As discussed in the model development section, δB_e is expected to absorb, at high frequencies, the effect of the stress drop variability. Figure 5 shows that the correlation between δB_e and $\Delta\sigma$ is significant at 10 Hz, whereas the correlation is low at 0.75 Hz. It is worth noting that the mainshocks and the

largest aftershocks deviate from the average correlation trend defined by the aftershock population. We ascribe this behavior to the fact that while $\Delta\sigma$ varies over three order of magnitude for small events, it is almost constant for earthquakes above magnitude 5. Since GMPE well describe the average the ground shaking generated by the largest magnitudes, their δB_e are distributed close to zero (Figure 3). The correlation of δB_e with $\Delta\sigma$ is also highlighted in Figure S4 of the electronic supplement where large positive residuals are associated to events with $\Delta\sigma$ higher than 0.6 MPa (i.e., the population average; Bindi et al., 2018) while earthquakes with lower stress drop have negative residuals. Figure 5 also shows the dependence of δB_e on hypocentral depth. The observed trend is reflecting the $\Delta\sigma$ dependences on depth as shown in Figure 2. The degree of correlation measured in terms of Pearson coefficient (Figure 6) confirms that the correlation is strongest around 10 Hz. The decrease of correlation toward low frequencies reflects the diminishing importance of $\Delta\sigma$ in determining the spectral amplitudes at frequencies lower than the corner one while the reduction above 10 Hz suggests that source-related effects other than the stress drop also affect the ground motion variability at high frequencies. The high frequencies radiations depends on many factors: small scale slip heterogeneity/slip roughness (Causse et al., 2010), rupture velocity and slip source function (Mai et al., 2017) and near source attenuation (Purvance and Anderson, 2003). For example, analyzing a smaller data set, Bindi et al. (2017) found a correlation between δB_e and the slope at high frequency of the acceleration source spectrum.

Stress drop temporal variability

The stress-drop variability with time (Figure 7a) resembles the variability observed for δB_e. If the earthquakes are grouped according to the latitude of their epicenters as shown in Figure 1, and focusing on the average trend, we observe that:

- $\Delta\sigma$ of earthquakes located in the L'Aquila region (Figure 7b) rapidly diminishes during the first month after the mainshock on April 6; the recovery starts after about two months (see also Figure 8a);

- for events located in the Campotosto segment (Chiaraluce et al., 2011) (Figure 7c), the recovery of the logarithm of $\Delta\sigma$ develops over a time span of 4 years, from 2010 to 2013, at an annual rate of 0.17 (i.e., the amplification factor for $\Delta\sigma$ is 1.5 per year). We recall that the Campotosto segment includes the northernmost termination of the 2009 sequence and the southern tip of the 2016 fault system (Chiaraluce et al., 2017). In particular, the four events with magnitude larger than 5 occurred in January 2017 are characterized by large $\Delta\sigma$ (see Figure 8), as for the largest aftershocks occurred over this segment during the 2009 sequence.

- a decrease in $\Delta\sigma$ is observed at the beginning of 2014, although no large earthquakes occurred at that time. Figure 9 shows the results of a breakpoint analysis (Bai, 1994; Zeileis et al., 2002; 2003) performed to detect changes in the coefficients of the linear regression with time. The analysis identifies a change-point within the period February 10 -

March 8, 2014 across which the slope of the logarithm of $\Delta\sigma$ with time reduce from $4.7e^{-04}$ to $9.4e^{-05}$ (the amplification factor per year for $\Delta\sigma$ reduces from 1.5 to 1). A detailed description of the breakpoint analysis is reported in the electronic supplement to this article. The cause driving this drop are not known. No large earthquakes occurred in the area around February-March 2014; the only notable event is the Gubbio swarm (Gualandi et al., 2017). At this stage, it is difficult to assess the plausibility of its involvement in the process we are examining here. Possible connections with the seismic and aseismic moment released during the 2013-14 Gubbio swarm are worth to be the subject of future work.

- earthquakes located in the northern group (Figure 7d) mainly belong to the 2016-17 Amatrice-Norcia-Visso sequence (Chiaraluce et al., 2017); also for these events, $\Delta\sigma$ is larger for the mainshocks and for the aftershocks above magnitude 5.5 (Figure S5 in the electronic supplement), and decreases after the mainshock occurrence (Figure 8c). The events occurred in this area before the 2016-17 sequence follow the same trends observed for the Campotosto segment.

Discussions and conclusions

The between-event residuals δB_e computed for ten years of data in central Italy show significant temporal variability at high frequency (Figure 4). On one hand, the time dependency of δB_e imply temporal changes of the ground shaking that could have an impact over the short term hazard. In the first

couple of months, δB_e at 10 Hz varies in the range from -1 to 1, roughly (i.e., about a factor 0.7 for spectral amplitudes); after a couple of months from L' Aquila mainshock, a trend develops with δB_e increasing on average from about 0 to 0.8, (i.e., about factor 2 in high frequency spectral content). On the other hand, Figure 7 shows that the high-frequency between-events variability resembles the time variability of the stress drop $\Delta\sigma$. Temporal variability of $\Delta\sigma$ has been observed in previous studies. For example, Abercrombie (2014) analyzed 25 earthquakes in three repeating sequences on the San Andreas at Parkfield, observing a long term gradual increase of $\Delta\sigma$ before the 2004 magnitude 6 earthquake. The values show an immediate decrease after the mainshock occurrence before recovering to previous values. Using a long-term stress drop catalog, Chen and Shearer (2013) found relatively stable long-term average stress drop in Southern California but a slow increase trend after large main shocks within the Landers fault zone was also identified, in agreement with a possible long-term fault zone recovery (Li et al., 1998).

Fault healing has been shown to promote the generation of high-frequency earthquakes both in laboratory experiments and on natural faults (e.g., Marone, 1998; McLaskey et al., 2012, Scuderi et al., 2016). The connection between pore pressure and effective normal stress has been also advocated to explain the time variability of the stress strop. Recently, Yoshida et al. (2017) analyzed a swarm triggered by the 2011 Tohoku earthquake, evaluating temporal changes in stress drop and b-value. They discussed the temporal variations of stress drop (very similar patterns to those observed in this study) in terms of changes in the frictional strength due to fluid

migration. In central Italy, pore pressure diffusion due to fluids migration played a role in the preparatory phase of the L'Aquila mainshock (e.g., Di Luccio et al 2010). However, pore pressure diffusion generally occurs over time scales of weeks to months. Thus, we reckon it is difficult to attribute solely to migration of fluids or pore pressure the variations we observe, which occur over time scales of several years.

Among other techniques, monitoring changes in seismic velocities has been shown to be effective in detecting fault healing and reloading processes (e.g., Brenguier et al., 2008; Chen et al., 2010). For example, Peng and Ben-Zion (2006) investigated the temporal variations of seismic velocity along the north Anatolian fault analyzing repeating earthquake clusters in the aftershock zones of the 1999 Izmit and Düzce earthquakes. The authors observed a sharp seismic velocity reduction immediately after the Düzce main shock, followed by a gradual logarithmic-type recovery. They concluded that the temporal changes of material properties occur in the topmost portion of the crust and, although the change is more prominent at stations located close to recently ruptured fault zones, it is not limited to the immediate vicinity of the fault zone. In central Italy, Soldati et al (2015) computed the relative velocity variation from cross-correlations of noise data over the period 2008-2012, including the 2009 L'Aquila main shock. The temporal variation obtained for the relative velocity (reproduced in Figure 10) has a trend very similar to the stress drop: an abrupt co-seismic decrease at the time of the main shock occurrence, followed by an unstable behavior for a few months and, finally, a recovery of the velocity (see also in Figure 7c). Regarding the spatial distribution of the co-seismic velocity drop, Soldati

et al. (2015) compared the velocities changes averaged over a one-month time window selected before and after the main shock occurrence, and excluding the day of the main shock. They found (see their Figure 5) that the drop was maximum over the area surrounding the L'Aquila epicentre and in the northeast direction from the fault zone, including the Campotosto area. The similarities of the trends observed for the stress drop and for the relative velocity variations suggest that, in agreement with Heckels et al (2018), the recovery can be associated both to crack-healing along the main fault system and to healing of micro-cracks distributed at shallow depths throughout the surrounding region.

Data and Resources

The R software (R Development Core Team, 2008; http://www.R-project.org) has been used in this study to perform the regressions. In particular, the packages lme4 (Bates et al., 2015; https://cran.r-project.org/web/ packages/lme4/news.html); ggplot (Wickham, 2009; http://ggplot2.org); changepoint (Killick,R., & Eckley, I.A., 2014; https://www.jstatsoft.org/article/view/v058i03); strucchange (Zeileis et al., 2002; http://www.jstatsoft.org/v07/i02/). The waveforms used in this study have been downloaded from European Integrated Data Archive-EIDA (https://www.orfeus-eu.org/data/eida/) and from the Italian Civil Protection (DPC) repository (http://ran.protezionecivile.it/IT/index.php). Regarding the permanent networks, we used data from the networks with FDSN code: MN, IV, IT (http://www.fdsn.org/networks/). The moment magnitude used in this study for all earthquakes larger than 5.7

have been taken from the Geofon moment tensor catalog (http://geofon.gfz-potsdam.de/eqinfo/ list.php?mode=mt). Only for L'Aquila mainshock, we used the GCMT solution (http://www.globalcmt.org/ CMTsearch.html). The earthquake locations are taken from the INGV bulletin (http://cnt.rm.ingv.it/iside). All the Internet sites have last accessed on December 2017. Some of the Figures were prepared with GMT (Wessel and Smith, 1991).

Acknowledgments

This study has been partially funded by the H2020 project SERA (Seismology and Earthquake Engineering Research Infrastructure Alliance for Europe). Comments from two anonymous Reviewer and the Associate Editor M. Chapman are strongly acknowledged. We thank L. Zaccarelli, G. Soldati and L. Faenza for providing their results on velocity variations used in Figure 10.

References

Abercrombie, R.E. (2014).Stress drops of repeating earthquakes on the San Andreas Fault at Parkfield, *Geophys. Res.Lett.* **41**, 87848791, doi:10.1002/2014GL062079.

Aki, K., (1967). Scaling law of seismic spectrum, *J. geophys. Res.* **72**, 12171231.

Ameri, G., S. Drouet, P. Traversa, D. Bindi and F. Cotton (2017). Toward an empirical ground motion prediction equation for France: accounting for regional differences in the source stress parameter, *Bull. Earthquake Eng.*

388 **15**, 46814717, DOI 10.1007/s10518-017-0171-1

389 Anderson, J. G., and Y. Lei (1994). Nonparametric Description of Peak
390 Acceleration as a Function of Magnitude, Distance, and Site in Guerrero,
391 Mexico, *Bull. Seismol. Soc. Am.* **84**, no. 4, 1003-1017

392 Bai J. (1994). Least Squares Estimation of a Shift in Linear Processes,
393 *Journal of Time Series Analysis*, **15**, 453-472

394 Baltay, A. and T.C. Hanks (2014). Understanding the magnitude de-
395 pendence of PGA and PGV in NGAWest 2 data, *Bull. Seism. Soc. Am.*
396 **104**, 2851-2865, https://doi.org/10.1785/0120130283

397 Baltay, A., T. C. Hanks, and N. A. Abrahamson (2017). Uncertainty,
398 Variability, and Earthquake Physics in Ground-Motion Prediction Equa-
399 tions, *Bull. Seismol. Soc. Am.* **107**, no. 4, doi: 10.1785/0120160164.

400 Bates D., M. Maechler, B. Bolker, and S. Walker (2015). Fitting Linear
401 Mixed-Effects Models Using lme4. *Journal of Statistical Software* **67**, 1,
402 1-48.

403 Bindi D., S. Parolai, H. Grosser, C. Milkereit, and E. Durukal (2007).
404 Empirical ground-motion prediction equations for northwestern Turkey us-
405 ing the aftershocks of the 1999 Kocaeli earthquake, *Geophys. Res. Lett.* **34**,
406 no. 8, doi: 10.1029/2007GL029222.

407 Bindi, D., Spallarossa, D. and F. Pacor (2017). Between-event and
408 between-station variability observed in the Fourier and response spectra
409 domains: comparison with seismological models, *Geophys. J. Int. 210*, doi:
410 10.1093/gji/ggx217

411 Bindi, D., Spallarossa, D., Picozzi M., Scafidi, D., and F. Cotton (2018).
412 Impact of Magnitude Selection on Aleatory Variability Associated with

413 Ground-Motion Prediction Equations: Part ILocal, Energy, and Moment
414 Magnitude Calibration and Stress-Drop Variability in Central Italy, *Bull.*
415 *Seism Soc. Am.*, doi: 10.1785/0120170356

416 Boore, D. M., and Atkinson, G. M., (1989). Spectral scaling of the 1985-
417 1988 Nahanni, Northwest Territories, earthquakes, *Bull. Seism Soc. Am.*
418 **79**, 17361761.

419 Brenguier, F., M. Campillo, C. Hadziioannou, N. M. Shapiro, R. M.
420 Nadeau, and E. Larose (2008), Postseismic relaxation along the San Andreas
421 Fault at Parkfield from continuous seismological observations, *Science*, **321**,
422 14781481, doi:10.1126/science.1160943.

423 Brune, J.N., (1970). Tectonic stress and the spectra of shear waves from
424 earthquakes, *J. geophys. Res.*, **75**, 49975009.

425 Castro, R. R., Anderson, J.G. and Singh, S.K., (1990). Site response,
426 attenuation and source spectra of S waves along the Guerrero, Mexico, sub-
427 duction zone, *Bull. Seism Soc. Am.*, **80**, 14811503.

428 Causse, M., Cotton, F., and Mai, P. M. (2010). Constraining the rough-
429 ness degree of slip heterogeneity. *J. Geophys. Res.: Solid Earth* **115(B5)**,
430 doi:10.1029/2009JB006747

431 Chen, J. H., Froment, B., Liu, Q. Y. and Campillo, M. (2010). Distribu-
432 tion of seismic wave speed changes associated with the 12 May 2008 Mw 7.9
433 Wenchuan earthquake. *Geophys. Res. Lett.* **37**, L18302, doi:10.1029/2010GL044582

434 Chen, X. and P. M. Shearer (2013). California foreshock sequences
435 suggest aseismic triggering process, *Geophys. Res. Lett.* **40**, 26022607,
436 doi:10.1002/grl.50444

437 Chiaraluce, L., L. Valoroso, D. Piccinini, R. Di Stefano, and P. De Gori

438 (2011). The anatomy of the 2009 LAquila normal fault system (central Italy)
439 imaged by high resolution foreshock and aftershock locations, *J. Geophys.*
440 *Res.***116**, no. B12, doi: 10.1029/2011JB008352.

441 Chiaraluce, L., R. Di Stefano, E. Tinti, L. Scognamiglio, M. Michele, E.
442 Casarotti, M. Cattaneo, P. De Gori, C. Chiarabba, G. Monachesi, A. Lom-
443 bardi, L. Valoroso, D. Latorre, and S. Marzorati (2017). The 2016 Central
444 Italy Seismic Sequence: A First Look at the Mainshocks, Aftershocks, and
445 Source Models, *Seismol Res Lett* **88**, no 3, doi: 10.1785/0220160221

446 Cotton, F., R. Archuleta, and M. Causse (2013). What is sigma of the
447 stress drop?, *Seismol. Res. Lett.* **84**, 4248, doi:10.1785/0220120087.

448 De Gori, P., F. P. Lucente, and C. Chiarabba (2015), Stressing of fault
449 patch during seismic swarms in central Apennines, Italy, *Geophys. Res.*
450 *Lett.* **42**, 21572163, doi:10.1002/2015GL063297.

451 Di Luccio, F., Ventura, G., Giovambattista, R.D., Piscini, A. and Cinti,
452 F.R., (2010). Normal faults and thrusts reactivated by deep fluids: the 6
453 April 2009 Mw 6.3 L'Aquila earthquake, central Italy, *J. geophys. Res.* **115**,
454 B06315, doi:10.1029/2009JB007190.

455 Eshelby, J. D. (1957). The determination of the elastic field of an el-
456 lipsoidal inclusion and related problems, *Proc. R. Soc. London A* **441**,
457 376396.

458 Gualandi, A., C. Nichele, E. Serpelloni,L. Chiaraluce, L. Anderlini, D.
459 Latorre,M. E. Belardinelli, and J.-P. Avouac (2017), Aseismic deformation
460 associated with an earthquake swarm in the northern Apennines (Italy),
461 *Geophys. Res. Lett.* **44**, 77067714, doi:10.1002/2017GL073687.

462 Hanks, T.C., and H. Kanamori (1979). A moment-magnitude scale, *J.*

geophys.Res. **84**, 23482350

Heckels,R.E.G., M. K. Savage and J. Townend (2018). Postseismic velocity changes following the 2010 Mw 7.1 Darfield earthquake, New Zealand, revealed by ambient seismic field analysis, *Geophys. J. Int*, ggy021, https://doi.org/10.1093/gji/ggy021

Keilis-Borok, V. (1959). On the estimation of the displacement in an earthquake source and of source dimension, *Ann. Geofisc.* **12**, 205214.

Killick,R., and Eckley, I.A., (2014). Changepoint: An R Package for Changepoint Analysis *J. of Statistical Software*, **58**,1-19

Konno, K, and T. Ohmachi (1998). Ground-motion characteristics estimated from spectral ratio between horizontal and vertical components of microtremor, *Bull Seismol Soc Am 88*, 228241

Li, Y. G., J. E. Vidale, K. Aki, F. Xu, and T. Burdette (1998). Evidence shallow fault zone strengthening after the 1992 M7.5 Landers, California earthquake, *Science* **279**, 5348, 217219.

Luzi L, Puglia R, Russo E and ORFEUS WG5 (2016). Engineering Strong Motion Database, version 1.0. Istituto Nazionale di Geofisica e Vulcanologia, Observatories & Research Facilities for European Seismology. doi: 10.13127/ESM

Mai, P. M., Galis, M., Thingbaijam, K. K., Vyas, J. C., and Dunham, E.M. (2017). Accounting for fault roughness in pseudo-dynamic ground-motion simulations. *Pure and Applied Geophysics*, **174**, 3419-3450.

Marone, C. (1998). The effect of loading rate on static friction and the rate of fault healing during the earthquake cycle, *Nature* **391**, 69-72

McLaskey, G. C., A. M. Thomas, S. D. Glaser and R. M. Nadeau

(2012).Fault healing promotes high-frequency earthquakes in laboratory experiments and on natural faults, *Nature* **491**, doi:10.1038/nature11512

Oth, A., Bindi, D., Parolai, S. and Di Giacomo, D., (2011). Spectral analysis of K-NET and KiK-net data in Japan, Part II: On attenuation characteristics, source spectra, and site response of borehole and surface stations, *Bull.seism. Soc. Am.* **101**, 2, 667- 687.

Oth, A., H. Miyake and D. Bindi (2017). On the relation of earthquake stress drop and ground motion variability, *J. Geophys. Res. Solid Earth* **122**, doi:10.1002/2017JB014026.

Pacor, F., Spallarossa, D., A. Oth, L. Luzi, R. Puglia, L. Cantore, A. Mercuri, M. D'Amico, and D., Bindi (2016). Spectral models for ground motion prediction in the L'Aquila region (central Italy): Evidence for stress-drop dependence on magnitude and depth, *Geophys. J. Int.*, **204**, 697718.

Peng,Z., and Y Ben-Zion (2006). Temporal changes of shallow seismic velocity around the Karadere-Dzce branch of the north Anatolian fault and strong ground motion *Pure and Applied Geophysics 163*, 567-600, doi 10.1007/s00024-005-0034-6

Piña-Valdés, J., A. Soquet, F. Cotton and S. Specht (2018). Spatio-temporal variations of ground motion in northern Chile before and after the 2014 Mw 8.1 Iquique megathrust, *Bull. Seism. Soc. Am.*, DOI: https://doi.org/10.1785/0120170052

Purvance, M. D., and Anderson, J. G. (2003). A comprehensive study of the observed spectral decay in strong-motion accelerations recorded in Guerrero, Mexico. *Bull.seism. Soc. Am.* **93**, 600-611.

R Development Core Team (2008). R: A language and environment

for statistical computing. R Foundation for Statistical Computing, Vienna, Austria. ISBN 3-900051-07-0

Scuderi, M. M., C. Marone, E. Tinti, G. Di Stefano, and C. Collettini (2016), Precursory changes in seismic velocity for the spectrum of earthquake failure modes, *Nat. Geosci.*, **9**, 695-700.

Soldati, G., L. Zaccarelli, L. Faenza and A. Michelini (2015). Monitoring of crustal seismic velocity variations in the LAquila fault zone inferred from noise cross-correlation, *Geophys. J. Int* **202**, 604-611, doi: 10.1093/gji/ggv172

Soquet, A., J. Piña-Valdés, J. Jara, F. Cotton, A. Walpersdorf, N. Cotte, S. Specht, F. Ortega-Culuciati, D. Carrizo and E. Norabuena (2016). An 8-month slow slip event triggers progressive nucleation of the 2014 Chile megathrust, Geophys. Res. Lett. **44**, 9, 4046-4053 doi: 10.1002/2017GL073023

Trugman, D. T., and P. M. Shearer (2018). Strong Correlation between Stress Drop and Peak Ground Acceleration for Recent M 14 Earthquakes in the San Francisco Bay Area , *Bull. Seism. Soc. Am.*, DOI: https://doi.org/10.1785/ 0120170245

Valoroso, L., Chiaraluce, L., Di Stefano, R., and Monachesi, G. (2017). Mixed-mode slip behavior of the Altotiberina low-angle normal fault system (Northern Apennines, Italy) through high-resolution earthquake locations and repeating events. *Journal of Geophysical Research: Solid Earth* **122**, 10,22010,240, doi:10.1002/2017JB014607

Wessel, P., and W. H. F. Smith (1991). Free software helps map and display data, *EOS Trans. Amer. Geophys. U.* **72**, no. 41, pp. 441, 445-446

Wickham, H. (2009). ggplot2: Elegant Graphics for Data Analysis.

Springer-Verlag New York, isbn 978-0-387-98140-6

Wooddell, K. E., and Abrahamson, N. A., (2014). Classification of main shocks and aftershocks in the NGA-West2 database, *Earthquake Spectra* **30**, 12571267

Wu, Q. and M. Chapman (2017). Stress-Drop Estimates and Source Scaling of the 2011 Mineral, Virginia, Mainshock and Aftershocks, *Bull. Seism. Soc. Am.* **107**, 2703-2720

Yoshida, K., T. Saito, Y. Urata, Y. Asano, A. Hasegawa (2017). Temporal changes in stress drop, frictional strength, and earthquake size distribution in the 2011 Yamagata-Fukushima, NE Japan, earthquake swarm, caused by fluid migration, *Journal of Geophysical Research: Solid Earth* **122**, 10,37910,397. https://doi.org/10.1002/2017JB014334

Zeileis A., Leisch F., Hornik K., Kleiber C. (2002) strucchange: An R Package for Testing for Structural Change in Linear Regression Models, *Journal of Statistical Software*, **7**, 2, 138

Zeileis,A., C. Kleiber, W. Krämer, and K. Hornik (2003) Testing and dating of structural changes in practic *Computational Statistics & Data Analysis*, **44**, 109-123

Figure captions

Figure 1. Map of earthquake epicenters (circles) analyzed in this study (see Data and Resources section). Circles are filled according to the latitude of the epicenter, assuming arbitrary thresholds at latitudes 42.4 and 42.68. A few earthquakes belonging to the 2014 Gubbio swarm are also included. The focal mechanisms of earthquakes with magnitude larger than 6 are shown as beach ball taken from Geofon and from the Global Centroid Moment Tensor catalogs (see Data and Resources section).The rectangles depict the surface projection of the faults as given in Luzi et al. (2016).

Figure 2. Scaling relationships between stress drop $\Delta\sigma$, hypocentral depth and moment magnitude Mw for the earthquakes analyzed in this study (Bindi et al., 2018). The trend-lines are estimated through a local regression (Loess) performed using the ggplot2 package in R (Wickham, 2009).

Figure 3. Observation minus prediction residuals versus predictor variables for the model in equation (1). The residual ϵ versus distance and the between event δB_e versus moment magnitude Mw are shown for the regressions performed at 0.75 Hz (left) and 10 Hz (right).

Figure 4. (a) Between-event residuals (δB_e) versus time, at 10 Hz. Earthquakes belonging to the Gubbio swarm (triangles; see Figure 1) are not considered for the evaluating the local-trend analysis; zooms over different time windows are presented in Figure S3 of the electronic supplements to this article. (b) Between-event versus time, at 0.75 Hz. (c) the same as in

(b) but zooming over the 2016 sequence. Vertical bars represent the 95% confidence interval for δB_e.

Figure 5. Between-event δB_e residuals versus stress drop $\Delta\sigma$ (top) and hypocentral depth (bottom), considering the results for 0.75 Hz (left) and 10 Hz (right).

Figure 6. Person correlation coefficients between $\Delta\sigma$ and δB_e at different frequencies.

Figure 7. Temporal variability of stress drop $\Delta\sigma$. (a) complete distribution of earthquakes; (b) only earthquakes located in proximity of the 2009 L' Aquila mainshock ; (c) only earthquakes occurred in the Campotosto segment; (d) earthquakes occurred in the area corresponding to the 2016-17 mainshocks. For the location of the earthquakes in panels (b) through (d), see Figure 1. Vertical bars represent the 95% confidence interval for $\Delta\sigma$. Zooms over different windows are available in Figure 8.

Figure 8. Temporal variability of stress drop $\Delta\sigma$, different zooms of Figure 7.

Figure 9. Results of the breakpoint analysis (Zeileis et al., 2002; 2003). A change in the linear trend with of $\Delta\sigma$ (dashed lines) is detected between February 10 and March 8, 2014 (vertical gray line). Details of the analysis are reported in the electronic supplements to this article.

Figure 10. Comparison between the relative shear wave velocity variation computed by Soldati et al (2015) (points) and the $\Delta\sigma$ (squares) time variability.

Figures

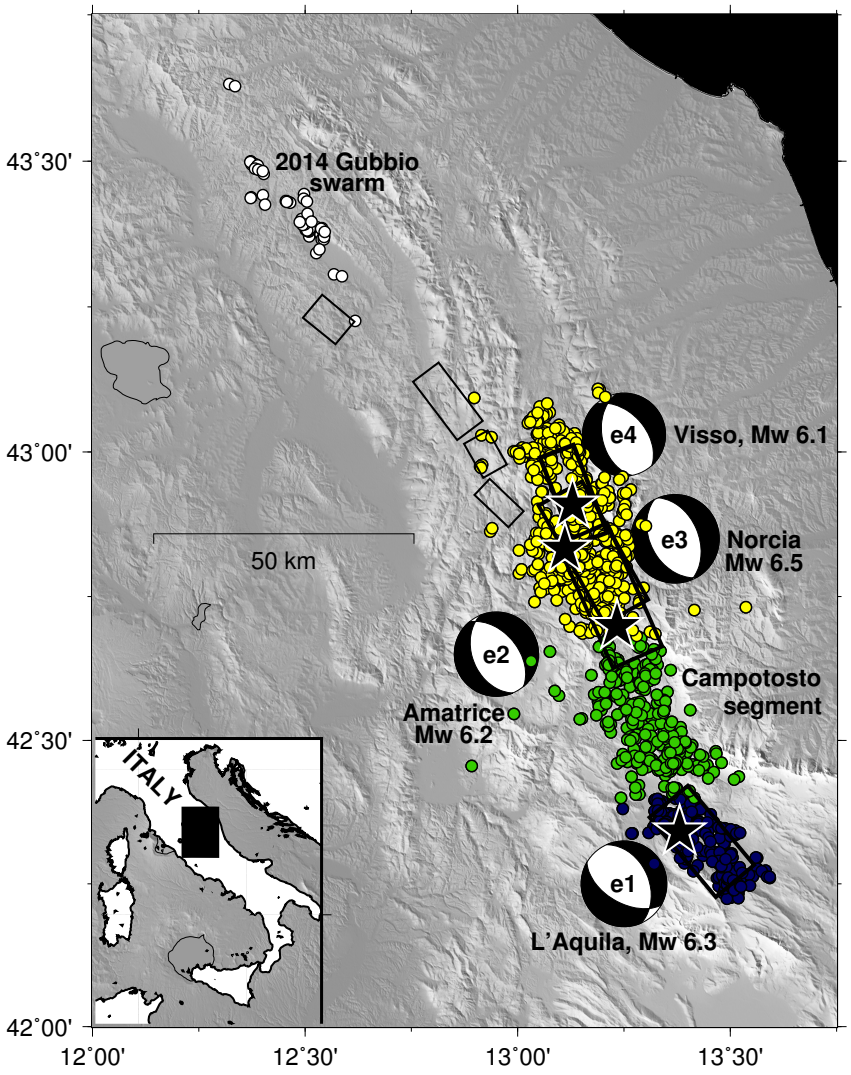
43˚30'
43˚00'
42˚30'
42˚00'
12˚00'
12˚30'
13˚00'
13˚30'
2014 Gubbio
swarm
e4
Visso, Mw 6.1
e3
Norcia
Mw 6.5
50 km
e2
Amatrice
Mw 6.2
Campotosto
segment
ITALY
e1
L'Aquila, Mw 6.3

Figure 1:

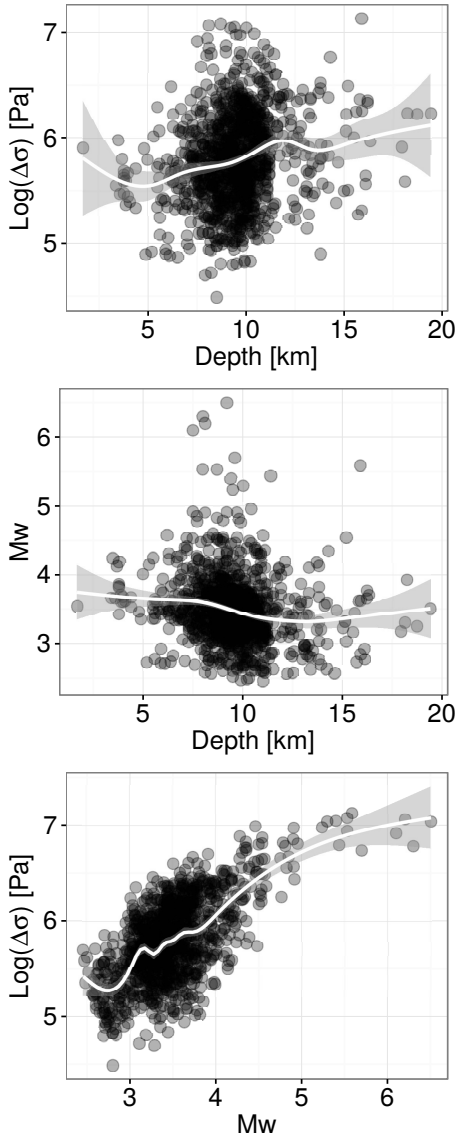
Log(Δσ) [Pa]
7
6
5
5
10
15
20
Depth [km]
Mw
6
5
4
3
5
10
15
20
Depth [km]
Log(Δσ) [Pa]
7
6
5
3
4
5
6
Mw

Figure 2:

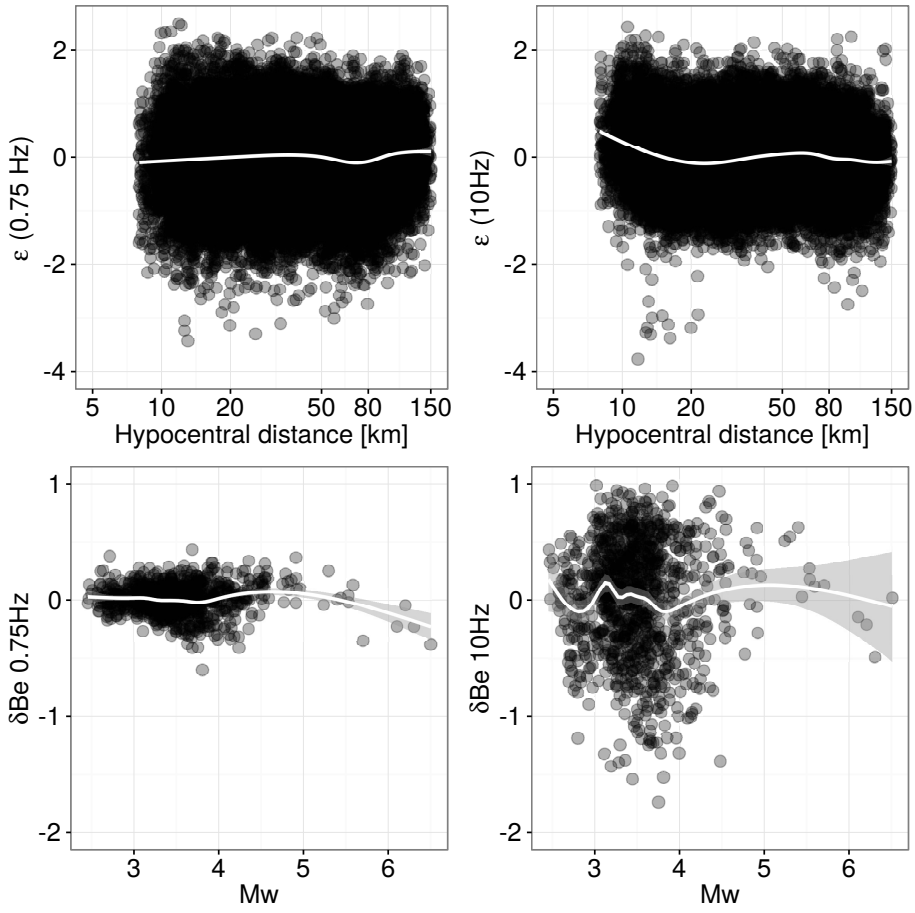
ε (0.75 Hz)
ε (10Hz)
Hypocentral distance [km]
Hypocentral distance [km]
δBe 0.75Hz
δBe 10Hz
Mw
Mw

Figure 3:

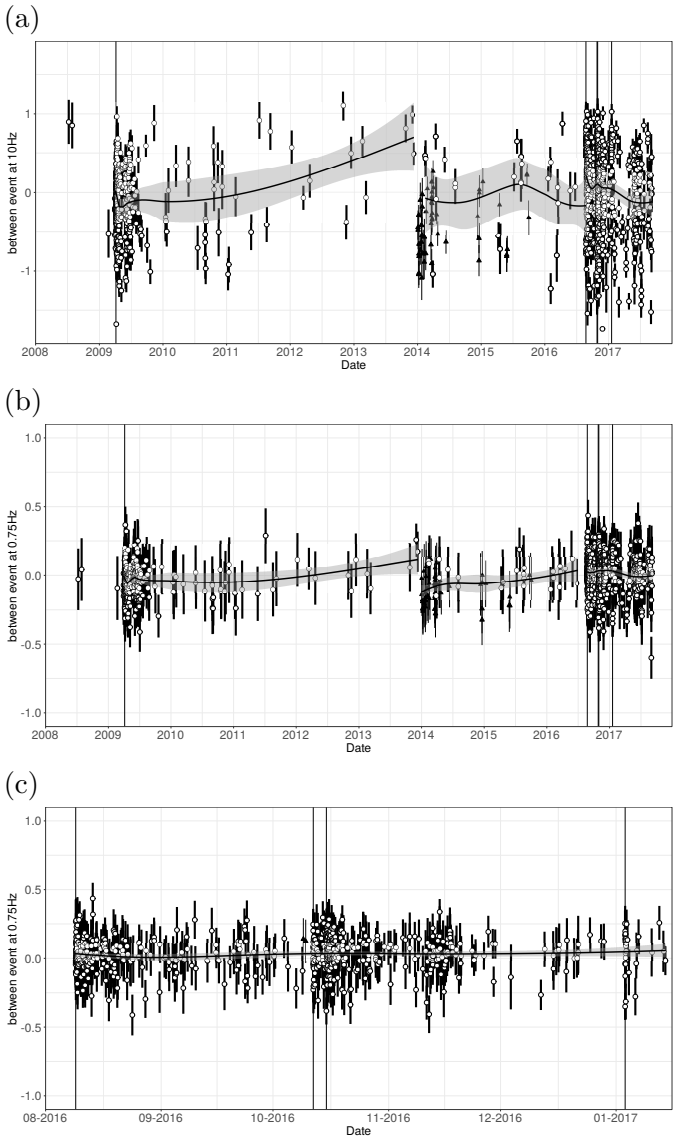
(a)
between event at 10Hz
1
0
-1
2008
2009
2010
2011
2012
2013
2014
2015
2016
2017
Date
(b)
between event at 0.75Hz
1.0
0.5
0.0
-0.5
-1.0
2008
2009
2010
2011
2012
2013
2014
2015
2016
2017
Date
(c)
between event at 0.75Hz
1.0
0.5
0.0
-0.5
-1.0
08-2016
09-2016
10-2016
11-2016
12-2016
01-2017
Date

Figure 4:

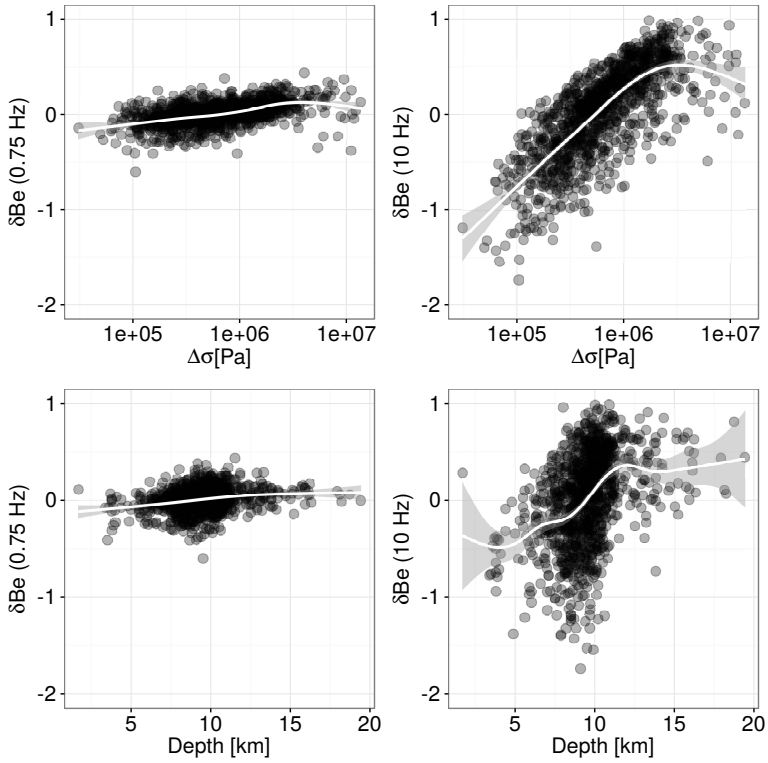

Figure 5:

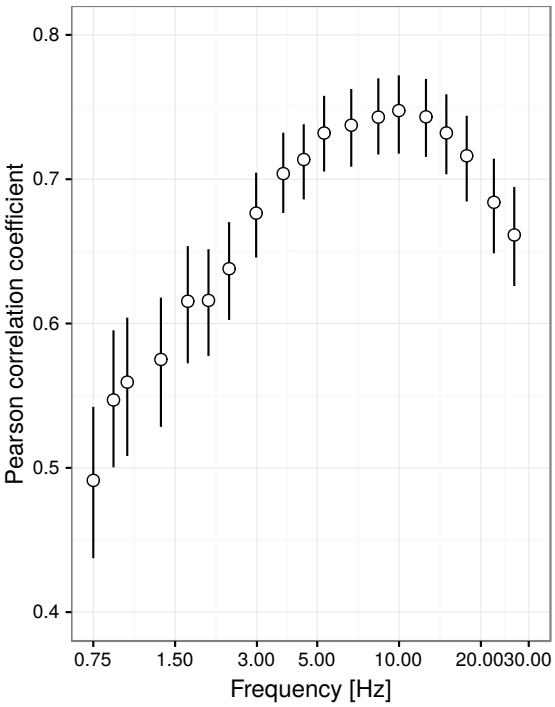
0.8
0.7
0.6
0.5
0.4
Pearson correlation coefficient
0.75
1.50
3.00
5.00
10.00
20.00
30.00
Frequency [Hz]

Figure 6:

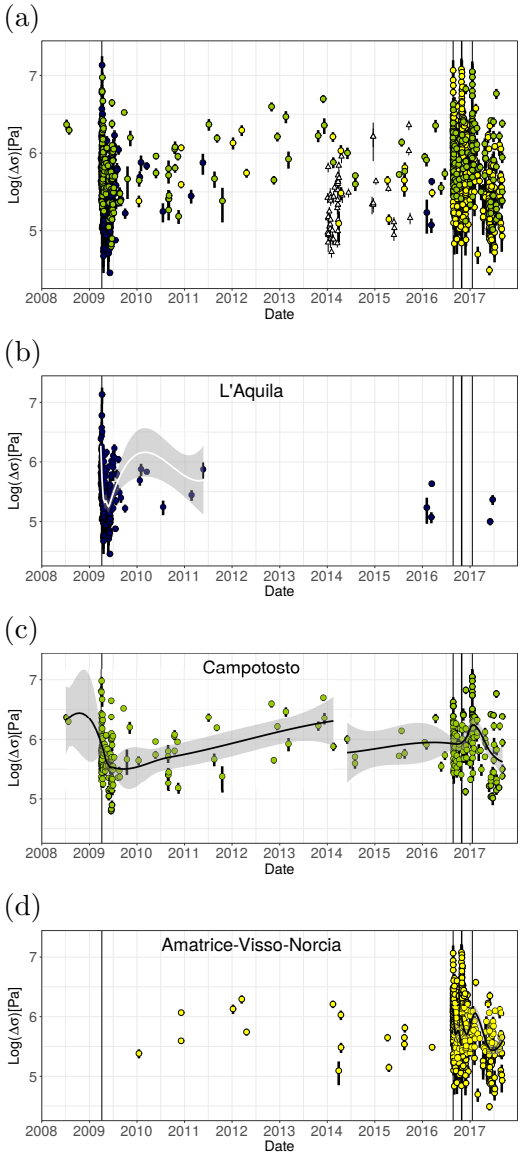
(a)
Log(Δσ)[Pa]
7
6
5
2008
2009
2010
2011
2012
2013
2014
2015
2016
2017
Date
(b)
L'Aquila
Log(Δσ)[Pa]
Date
(c)
Campotosto
Log(Δσ)[Pa]
Date
(d)
Amatrice-Visso-Norcia
Log(Δσ)[Pa]
Date

Figure 7:

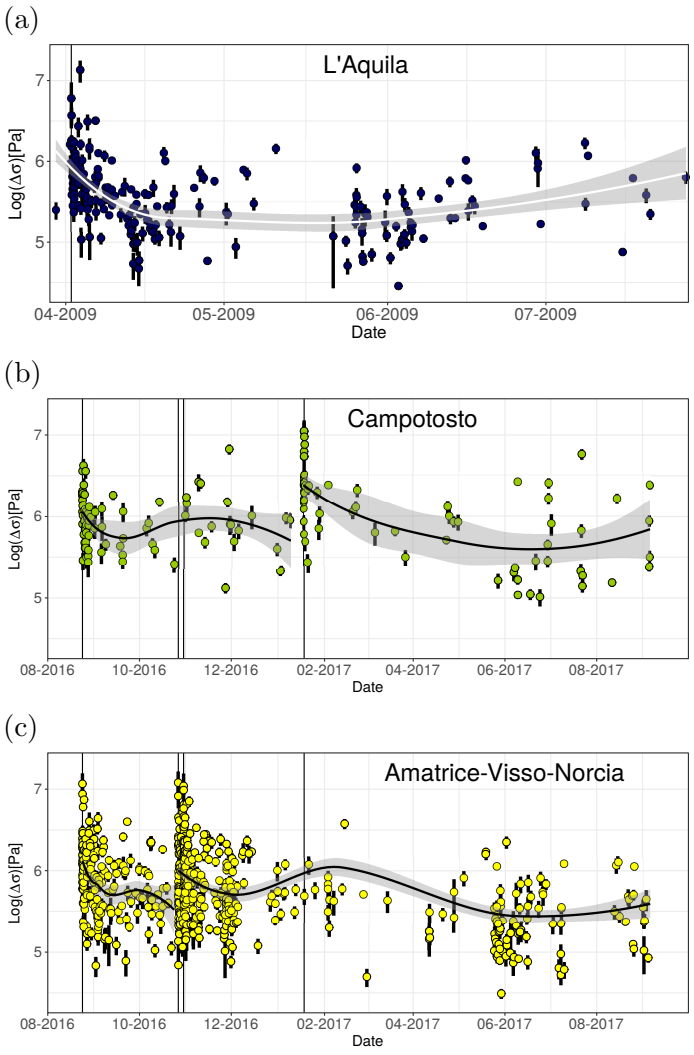
(a)
L'Aquila
Log(Δσ)[Pa]
7
6
5
04-2009
05-2009
06-2009
07-2009
Date
(b)
Campotosto
Log(Δσ)[Pa]
7
6
5
08-2016
10-2016
12-2016
02-2017
04-2017
06-2017
08-2017
Date
(c)
Amatrice-Visso-Norcia
Log(Δσ)[Pa]
7
6
5
08-2016
10-2016
12-2016
02-2017
04-2017
06-2017
08-2017
Date

Figure 8:

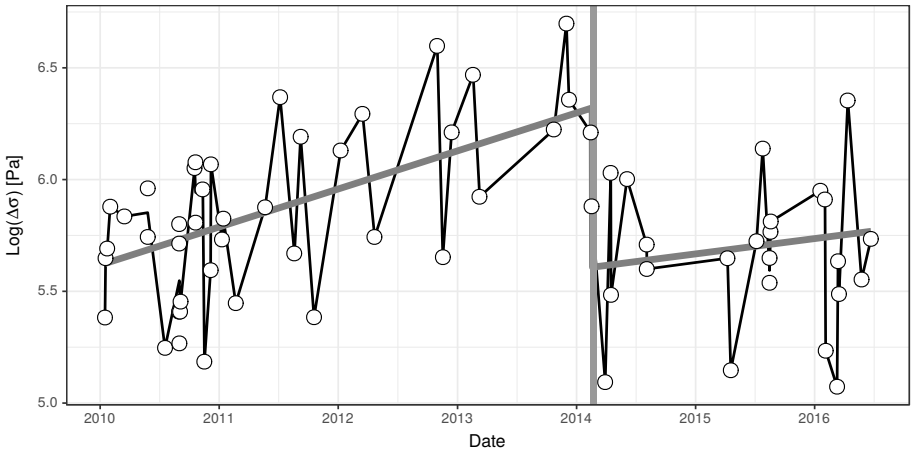

Figure 9:

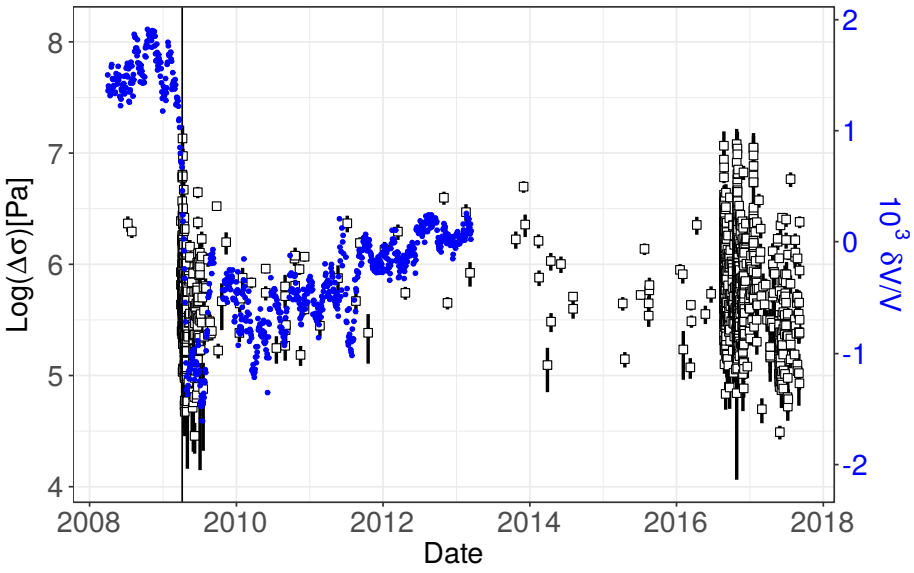
8
7
6
5
4
Log(Δσ)[Pa]
2008
2010
2012
2014
2016
2018
Date
2
1
0
-1
-2
10^3 δV/V

Figure 10:

Temporal variability of ground-shaking and stress drop in central Italy: a hint for fault healing?

D. Bindi, F. Cotton, D. Spallarossa, M. Picozzi, and E. Rivalta

This Supplementary Material includes additional Figures cited in the main article. In figure S1, a map with the locations of stations used in this study is provided. The map in Figure S2 shows the earthquake locations as in Figure 1 but with symbols filled according to the time elapsed since the L'Aquila earthquake. Figure S3 complements Figure 4 by showing the variability with time of the between event residuals δB_e at 10Hz considering different time windows. In Figure S4, the symbols used to depict the time dependency of δB_e at 10Hz are filled according to the logarithm of the stress drop $\Delta\sigma$, measured in [Pa]. Finally, in Figure S5, the symbols used to show the time variability of $\Delta\sigma$ are filled according to the moment magnitude Mw.
The Supplementary Material includes also Table S1, listing the frequency-dependent coefficients of the Ground Motion Prediction Equation developed in this study (equation 6) for the Fourier amplitude spectra. Finally, the Supplementary Material includes additional text describing both the error propagation applied for $\Delta\sigma$ and the break-point analysis performed for locating the $\Delta\sigma$ change-point occurred at the beginning of 2014.

Error propagation

The non-parametric source spectra *S(f)* obtained through the non-parametric Generalized Inversion (Bindi et al., 2017) are described in terms of acceleration source model (Brune, 1970):

$$S_{Brune}(f) = const M_0 \frac{f^2}{1+\left(\frac{f}{f_c}\right)^2} \quad \text{(S1)}$$

where M_o is the seismic moment, f_c the corner frequency and *const* is a constant depending on the radiation pattern, free surface amplification, density and velocity at the source location. We fit the $S_{Brune}(f)$ model to *S(f)* by computing the logarithm (hereinafter we refer to the logarithm in base 10 as *log* and to the natural logarithm as *ln*) of the spectra and considering as independent variables $log(M_o)$ and f_c. The fit is performed following a non-linear least-squares approach and the variance-covariance matrix *vCov* is evaluated. From the square root of the diagonal of *vCov*, we extracted the standard errors on f_c and on $log(M_o)$, referred to as δ_{fc} and δ_{logMo}, and from the off-diagonal elements the correlation between f_c and $log(M_o)$, indicated as $\delta_{(fc,logMo)}$. The error propagation is evaluated through the variance formula for correlated variables, truncated at the first order of the Taylor's expansion:

$$\delta^2_{\Delta\sigma} = \left(\frac{\partial\Delta\sigma}{\partial f_c}\right)^2 \delta^2_{f_c} + \left(\frac{\partial\Delta\sigma}{\partial log(M_o)}\right)^2 \delta^2_{logM_o} + 2\delta_{(f_c,LogM_o)} \frac{\partial\Delta\sigma}{\partial f_c} \frac{\partial\Delta\sigma}{\partial log(M_o)} \quad \text{(S2)}$$

The stress drop $\Delta\sigma$ is computed from M_o and f_c using the following relationships (Eshelby, 1957; Brune 1970):

$$\Delta\sigma = \frac{7}{16}\frac{M_o}{r^3} \quad \text{(S3)}$$

$$r = 2.34\frac{v_S}{2\pi f_c} \quad \text{(S4)}$$

where v_s is the shear-wave velocity at the source. Considering the logarithm of $\Delta\sigma$, equations (S3) and (S4) give

$$log(\Delta\sigma) = constant + log(M_o) + 3log(f_c) \quad \text{(S5)}$$

and equation (2) becomes

$$\delta^2_{log(\Delta\sigma)} = \left(\frac{\partial log(\Delta\sigma)}{\partial f_c}\right)^2 \delta^2_{f_c} + \left(\frac{\partial log(\Delta\sigma)}{\partial log(M_o)}\right)^2 \delta^2_{logM_o} + 2\delta_{f_c,logM_o} \frac{\partial log(\Delta\sigma)}{\partial f_c} \frac{\partial log(\Delta\sigma)}{\partial log(M_o)} \quad \text{(S6)}$$

From equation (5),

$$\frac{\partial log(\Delta\sigma)}{\partial log(M_o)} = 1 \quad \frac{\partial log(\Delta\sigma)}{\partial f_c} = \frac{3}{ln(10)}\frac{1}{f_c} \quad \text{(S7)}$$

Using (7) in (6), we obtain

$$\delta^2_{log(\Delta\sigma)} = \frac{9}{[ln(10)]^2}\left(\frac{\delta_{f_c}}{f_c}\right)^2 + \delta^2_{logM_o} + \delta_{(f_c,logM_o)} \frac{6}{ln(10)}\frac{1}{f_c} \quad \text{(S8)}$$

The error propagation in equation (S8) is similar to the one described by Cotton et al (2013), in their equation (9). The differences are related to a different choice of the variables, since they used $log(f_c)$ while we used f_c, and to the fact that Cotton et al (2013) neglected the cross-term of the covariance matrix. The advantage of using $log(f_c)$ is that equation (S5) becomes linear with respect to the variables and, therefore, equation (S2) is exact. The drawback is that in fitting the Brune model, the dependence on the variable takes the more complex form of $10^{log(fc)}$. Regarding the cross-term, since $\delta_{(fc,logMo)}$ is negative, the choice of Cotton et al (2013) was conservative.

Finally, since $\delta_{\Delta\sigma} = ln(10)\Delta\sigma\ \delta log(\Delta\sigma)$, from equation (S8) we get the standard error on $\Delta\sigma$

$$\delta_{\Delta\sigma} = \Delta\sigma\sqrt{9\left(\frac{\delta_{f_c}}{f_c}\right)^2 + [ln(10)]^2\delta^2_{logM_o} + \frac{6ln(10)}{f_c}\delta_{(f_c,logM_o)}} \quad \text{(S9)}$$

Figure S6 shows the 95% confidence interval, computed as 1.96 times the standard error, for the data analyzed in this study. Zooms over different time windows are shown in Figure S7.

Breakpoint analysis

In order to assess the statistical significance of the abrupt drop in $\Delta\sigma$ occurring at the beginning of 2014, we performed a change-point analysis (Page, 1954; Jaiswal et al., 2015). The analysis was performed though the following steps, outlined in Figure S8:

- we considered $\Delta\sigma$ values between January 2010 and June 2016 (Figure S8a);
- since the time series is unevenly sampled, we applied and interpolation scheme. After some tests using different approaches, we used a simple linear interpolation between consecutive samples. The time series interpolated using a regular sampling of 1 day is shown in Figure S8b;
- A preliminary detection in terms of significant change in the average was performed following the approach of Killick and Eckley (2014). The detected change point (Figure S8c) is located on February 15, 2014;
-finally, the breakpoint analysis of Zeileis et al (2003) was applied to identify and locate a change in the coefficients of the linear regression with time. Figure S8d shows the location of the change point with its 95% confidence interval (corresponding to the period from February, 10 to March, 8) and the best linear models before and after the change point.

Table caption

Table S1. Coefficients (e_1,b_1,b_2,c_1,c_2,c_3) of the Fourier ground motion prediction equation described in equation (6); ϕ_{S2S}, τ, ϕ_0 are the standard deviation of the between station δBs, of the between event δBe and residual ε distributions (see equation 6).

Figure captions

Figure S1 Location of stations considered in this study.
Figure S2 Location of earthquakes considered in this study with symbols filled according to the earthquake origin time with respect to April 6, 2009 (see also Figure 1).
Figure S3 Between-event residuals δBe versus time at 10 Hz for different time intervals (see also Figure 4).
Figure S4 Between-event residuals δBe versus time with symbols filled according to stress drop $\Delta\sigma$. Triangles indicate earthquakes occurred in the area of the 2013-14 Gubbio swarm, see Figure 1.
Figure S5 Stress drop $\Delta\sigma$ versus time with symbols filled according to moment magnitude Mw. Triangles indicate earthquakes occurred in the area of the 2013-14 Gubbio swarm, see Figure 1.
Figure S6. 95% confidence intervals for $\Delta\sigma$.
Figure S7. 95% confidence intervals for $\Delta\sigma$, for different time intervals.
Figure S8. Change point analysis. a) original data. b) data linearly re-sampled at the rate of one sample per day; c) detection of the change point for the average; d) detection of the change point in the linear regression coefficients

References

Cotton, F., R. Archuleta and M. Causse (2013). What is the sigma of stress drop, *Seism. Res. Lett*. **84**, 42-48 doi: 10.1785/0220120087

Jaiswal, R. K., Lohani A. K., and H. L. Tiwari (2015). Statistical analysis for change detection and trend, *Envirom. Process*, **2**, 729-749, doi: 10.1007/s40710-015-0101-3

Page, E. S. (1954). Continuous inspection schemes, *Biometrika*, **41**, 100-115 doi 10.1093/biomet/41.1-2.100

Table S1. Coefficients (e_1,b_1,b_2,c_1,c_2,c_3) of the Fourier ground motion prediction equation described in equation (6); ϕ_{S2S}, τ, ϕ_0 are the standard deviation of the between station δBs, of the between event δBe and residual ε distributions (see equation 6).

Freq [Hz]	e_1	b_1	b_2	c_1	c_2	c_3	ϕ_{S2S}	τ	ϕ_0
0.35	0.80146	2.21669	-0.04089	-2.00751	0.17379	0.00545	0.47522	0.21587	0.70041
0.4	1.04779	2.27639	-0.04779	-2.07823	0.17007	0.00764	0.47742	0.20514	0.6891
0.5	1.33959	2.42340	-0.06803	-2.12578	0.15654	0.00992	0.48835	0.18558	0.64771
0.59	1.56116	2.52567	-0.1043	-2.15865	0.14717	0.01189	0.51034	0.17384	0.6542
0.75	1.92521	2.68625	-0.15401	-2.18397	0.12672	0.01265	0.54612	0.14888	0.60759
0.89	2.33067	2.71259	-0.18884	-2.23543	0.1305	0.01312	0.57532	0.14129	0.58482
1	2.60114	2.72391	-0.21177	-2.27032	0.12893	0.01357	0.59266	0.14381	0.59366
1.33	3.09564	2.76270	-0.23556	-2.26438	0.10171	0.01225	0.61237	0.16665	0.56748
1.67	3.48468	2.68448	-0.24237	-2.27198	0.0962	0.01163	0.61487	0.19459	0.53169
1.99	3.67784	2.62330	-0.24584	-2.26209	0.0945	0.01103	0.6234	0.22036	0.53082
2.37	3.76324	2.55504	-0.23485	-2.20498	0.08715	0.00903	0.63017	0.25424	0.52461
2.98	3.59658	2.38582	-0.21798	-2.04151	0.0927	0.00468	0.60396	0.29829	0.52005
3.75	3.42988	2.25625	-0.19759	-1.90391	0.08802	0.00061	0.62728	0.34572	0.52529
4.46	3.28532	2.08639	-0.17907	-1.79832	0.10474	-0.00292	0.65699	0.37856	0.5284
5.3	3.07226	2.00030	-0.15746	-1.69606	0.09872	-0.00611	0.69546	0.40803	0.52817
6.67	2.87406	1.86515	-0.13773	-1.60836	0.10035	-0.00995	0.76182	0.44405	0.52234
8.39	2.57230	1.78698	-0.11523	-1.51731	0.08999	-0.01435	0.81647	0.48376	0.52027
10	2.36854	1.71378	-0.09805	-1.47415	0.08535	-0.01735	0.87734	0.51209	0.51604
12.56	2.31993	1.61380	-0.08088	-1.50875	0.08424	-0.02057	0.96463	0.56033	0.51112
14.93	2.34572	1.50170	-0.06593	-1.57316	0.09194	-0.02223	102.517	0.59434	0.51074
17.74	2.35082	1.44668	-0.03929	-1.67057	0.08297	-0.0224	108.441	0.63308	0.5131
22.33	2.52609	1.39944	-0.01618	-1.91863	0.06611	-0.01832	112.420	0.68558	0.52859
26.54	2.67305	1.39498	0.01618	-2.11285	0.04734	-0.01503	109.470	0.70831	0.52971

Supplemental Material (Main Page, Tables, Figures)

Click here to download Supplemental Material (Main Page, Tables, Figures) figure_S1.jpg

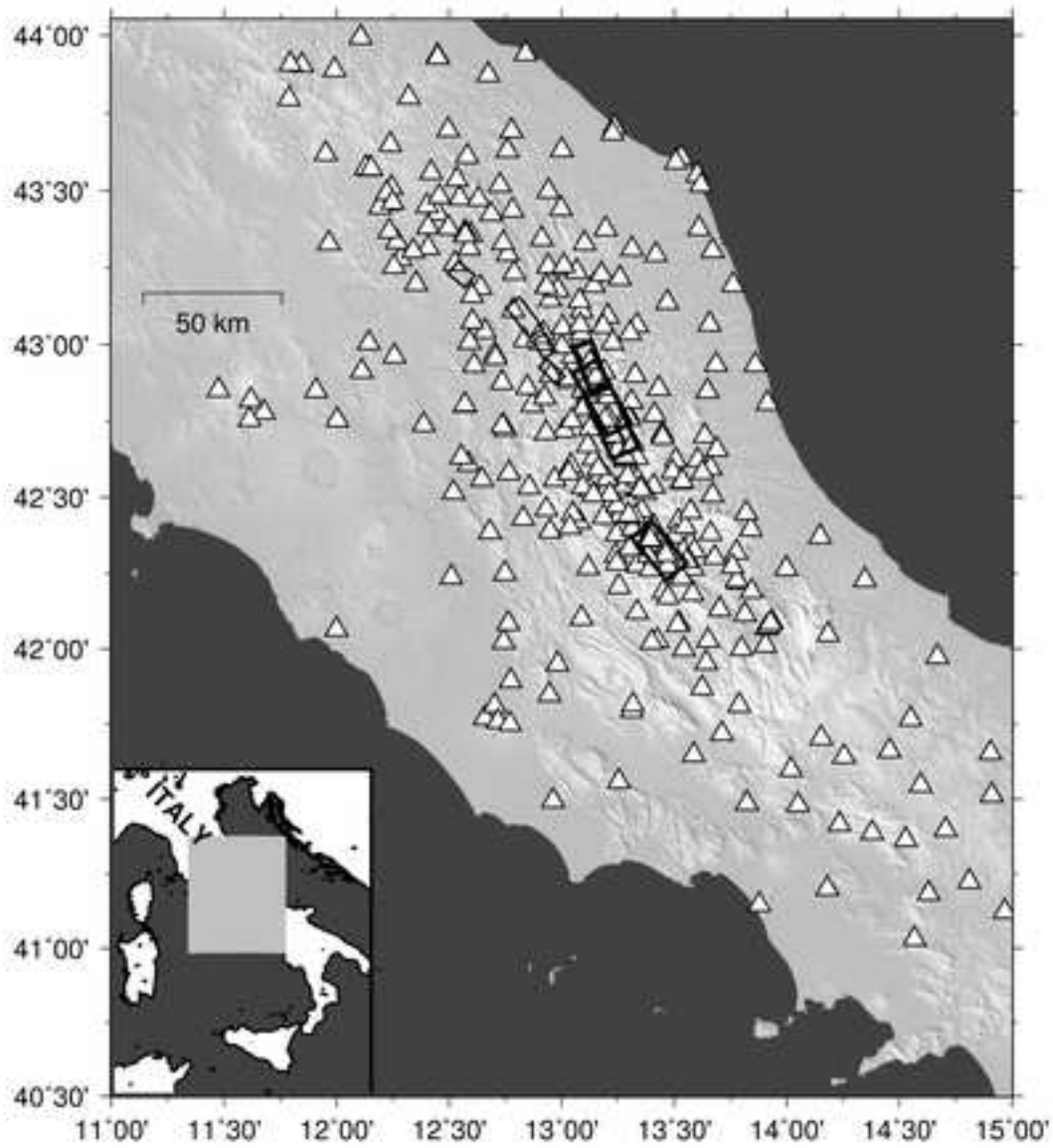

Supplemental Material (Main Page, Tables, Figures)

Click here to download Supplemental Material (Main Page, Tables, Figures) figure_S2.jpg

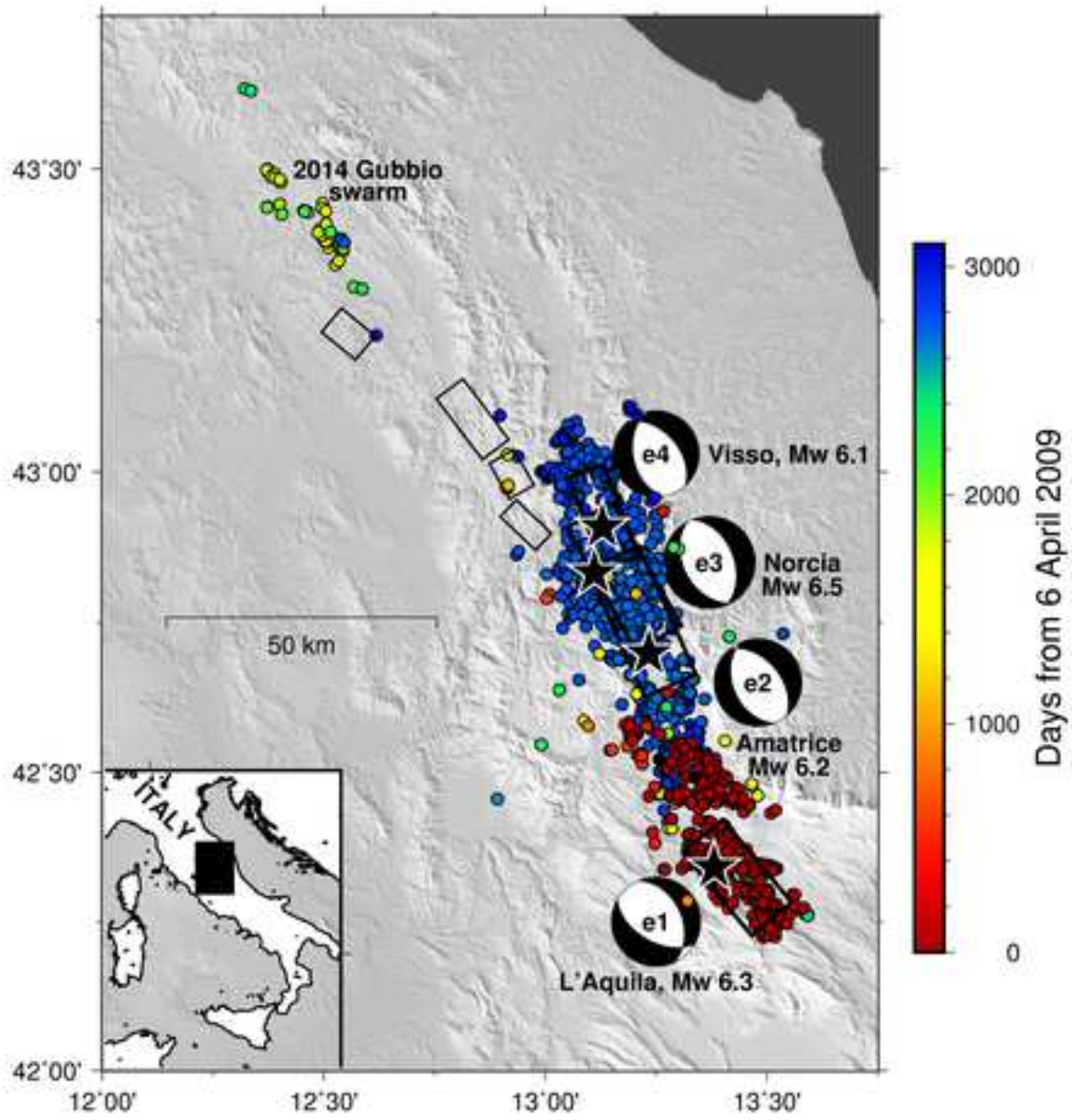

Supplemental Material (Main Page, Tables, Figures)

Click here to download Supplemental Material (Main Page, Tables, Figures)
figure_S3.jpg

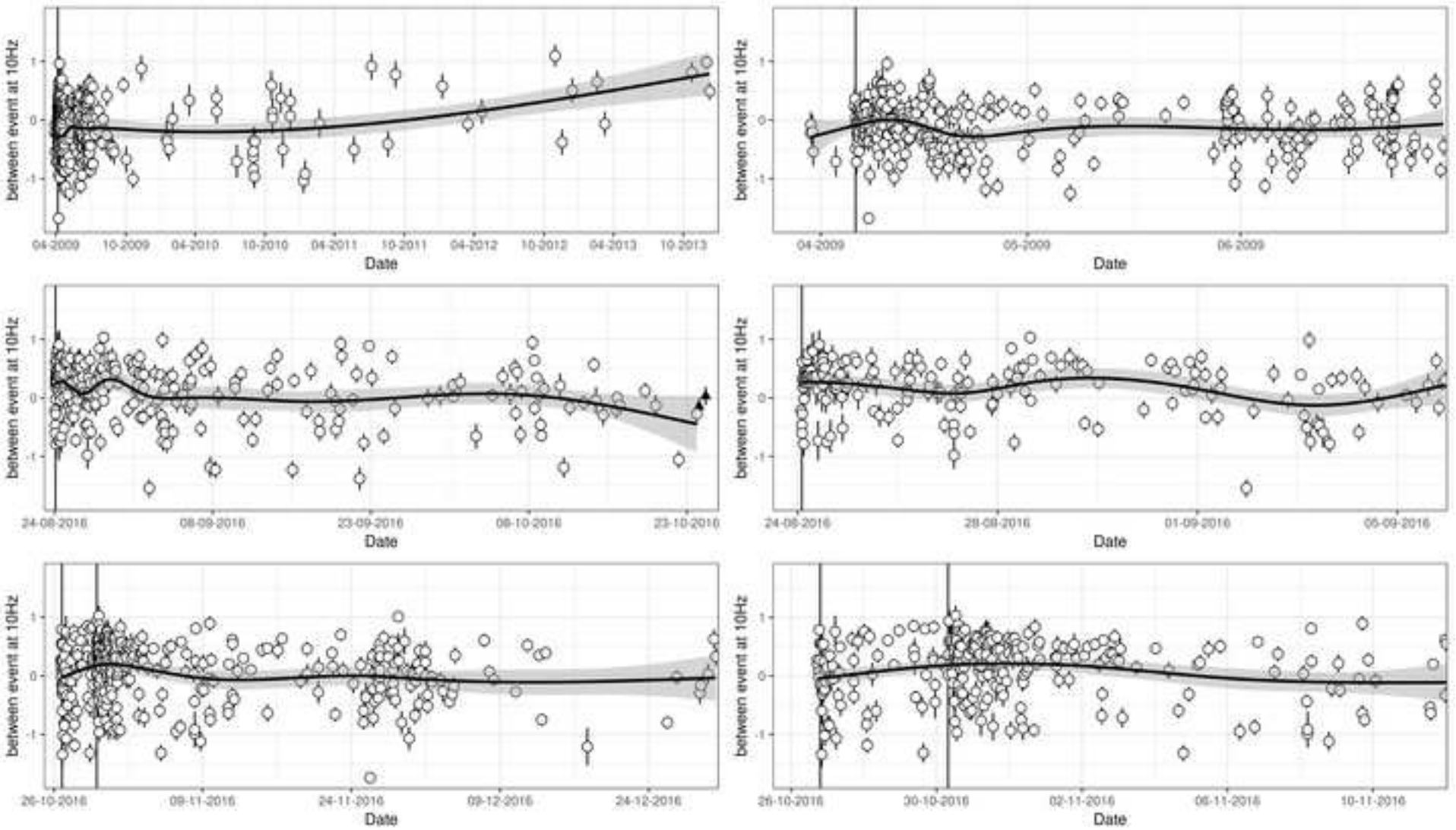

Supplemental Material (Main Page, Tables, Figures)

Click here to download Supplemental Material (Main Page, Tables, Figures)
figure_S4.jpg

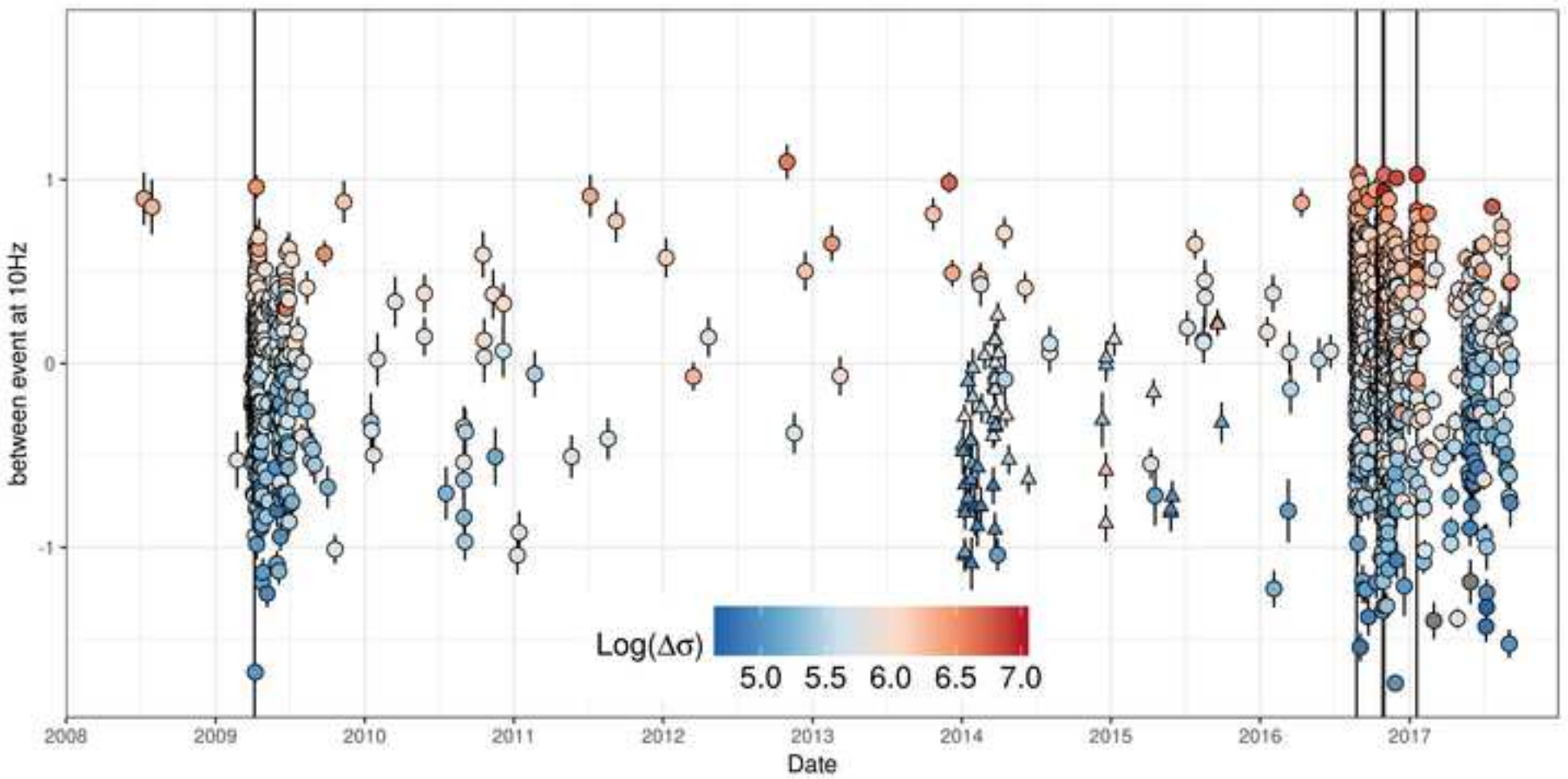

Supplemental Material (Main Page, Tables, Figures)

Click here to download Supplemental Material (Main Page, Tables, Figures)
figure_S5.jpg

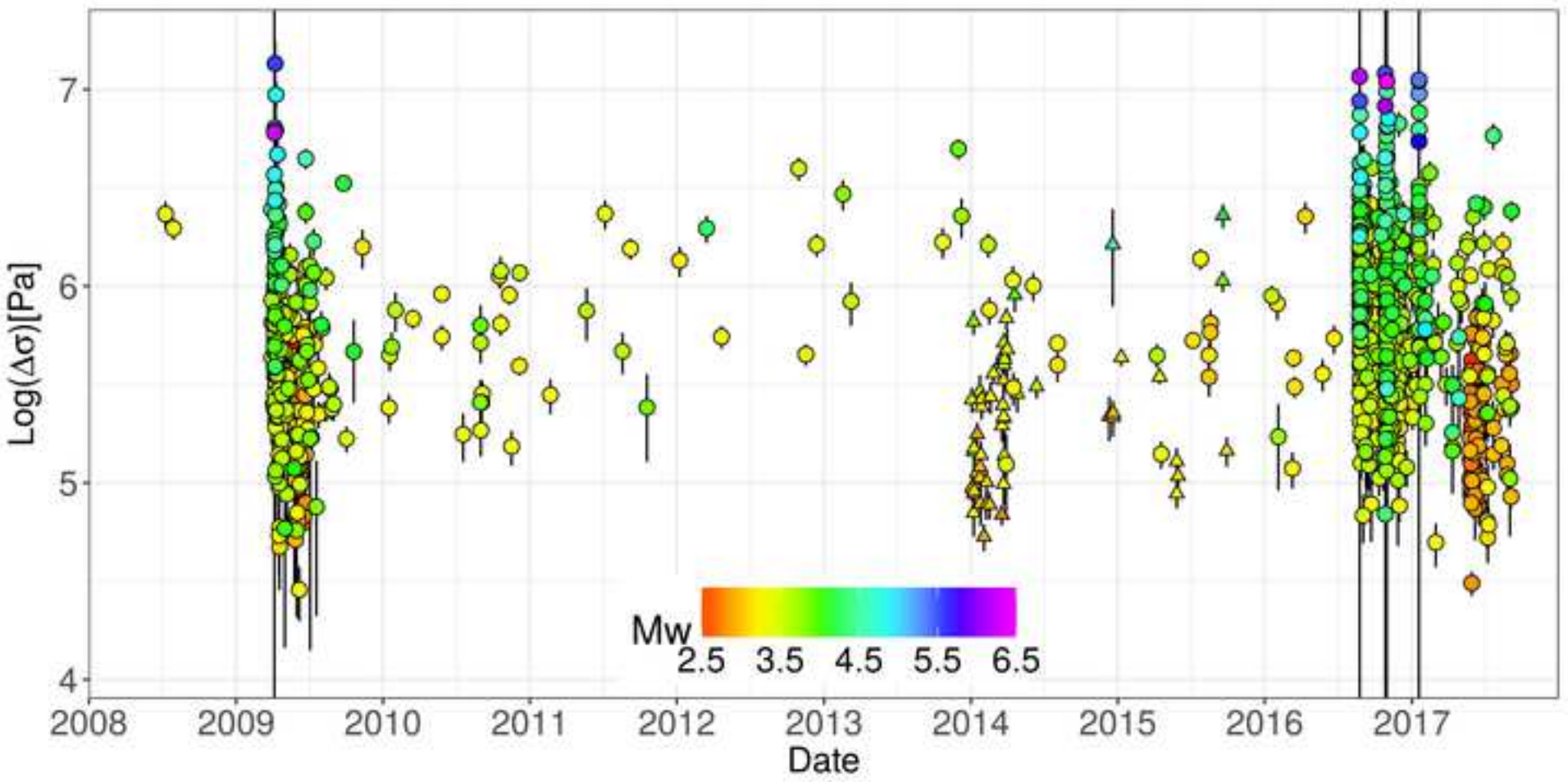

Supplemental Material (Main Page, Tables, Figures)

Click here to download Supplemental Material (Main Page, Tables, Figures) figure_S6.jpg

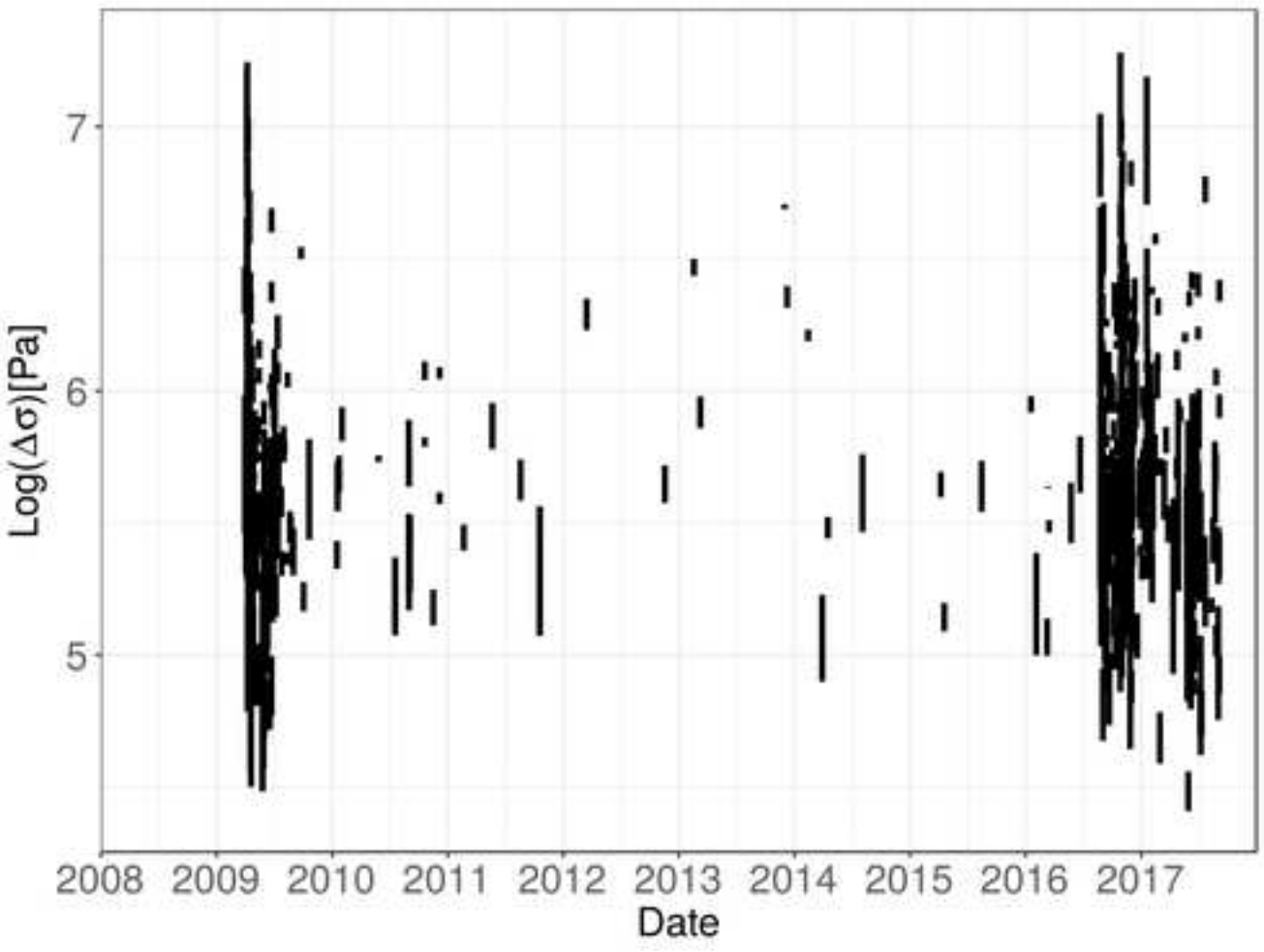

Supplemental Material (Main Page, Tables, Figures)

Click here to download Supplemental Material (Main Page, Tables, Figures) figure_S7.jpg

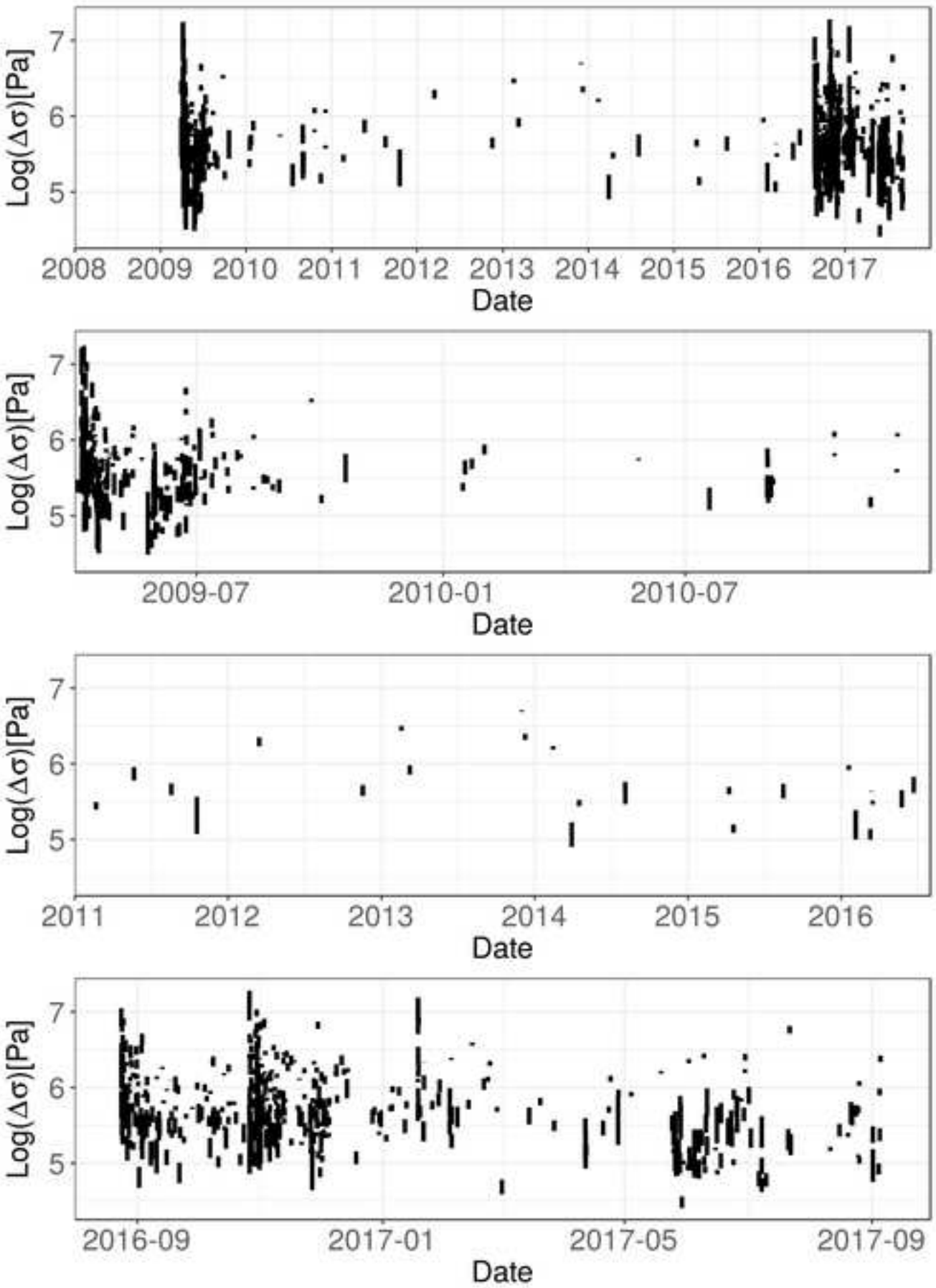

Supplemental Material (Main Page, Tables, Figures)

Click here to download Supplemental Material (Main Page, Tables, Figures) figure_S8.jpg